Mesoporous MnO2 hollow spheres for enhanced catalytic oxidation of formaldehyde

Yash Boyjoo, Guillaume Rochard, Jean-Marc Giraudon, Jian Liu,
Jean-Francois Lamonier

Mesoporous MnO₂ Hollow Spheres for Enhanced Catalytic Oxidation of Formaldehyde

Yash Boyjoo,[a] Guillaume Rochard,[a] Jean-Marc Giraudon,[a] Jian Liu [b,c*] and Jean-François Lamonier [a*]

[a] Univ. Lille, UMR CNRS 8181, UCCS – Unité de Catalyse et Chimie du Solide, F-59000 Lille, France

[b] Department of Chemical and Process Engineering, and Advanced Technology Institute, University of Surrey, Guilford, Surrey, GU2 7XH, UK.

[c] State Key Laboratory of Catalysis, iChEM, Dalian Institute of Chemical Physics, Chinese Academy of Sciences, 457 Zhongshan Road, Dalian 116023, China

Corresponding author: jian.liu@surrey.ac.uk , jean-francois.lamonier@univ-lille1.fr

Keywords: MnO₂, hollow spheres, formaldehyde, catalytic oxidation

Abstract

In this work, hollow MnO2 spheres were synthesized via a sacrificial templating method using SiO2 nanospheres as hard templates. The MnO2 coating on SiO2 was achieved by a newly devised low-temperature, controlled precipitation by redox (CPR) method which is based on the controlled redox reaction between KMnO4 and Mn (NO3)2 at 30 °C. After calcination of the SiO2@MnO2 core shell spheres at 300 °C, hollow spheres were obtained following template removal by NaOH etching. The hollow spheres were characterized by XRD, Raman spectroscopy, TEM, HRTEM, N2 adsorption, XPS and H2-TPR. Two different MnO2 crystal phases (γ- and δ-MnO2) could be obtained by making simple changes in the precursor addition

protocols during synthesis. All the samples had high BET surface areas between 104 m2 g−1 and 236 m2 g−1, hierarchical pore size distribution with high mesoporosity and the presence of oxygen vacancies for high mobility of oxygen species on the catalyst surface.

The catalysts were used for the complete catalytic oxidation of formaldehyde in dry air (100 ppmv; GHSV: 30,000 h−1). Long-term stability tests showed that γ-MnO2 deactivated gradually with time potentially due to structural collapse of the hollow spheres. The interlayer spacing in the δ-MnO2 sample, however, was responsible for increasing the expected conversion due to the regeneration of oxygen/hydroxyl species from adsorbed water formed from the oxidation of formaldehyde on the catalyst surface.

Keywords: MnO2, Hollow spheres , Formaldehyde, Catalytic oxidation

1. Introduction

Formaldehyde (HCHO) is a dangerous volatile organic compound (VOC) that is present in indoor environment such as houses, offices and schools. HCHO emanate from wood adhesives, furniture, antiseptics and disinfectants, textiles, dyes, cigarette smoke, etc. [1]. Its slow release in indoor air can be toxic and carcinogenic to humans, even from exposure to very low concentrations ranging from 3 ppb to 0.1 ppm [1]. Therefore, the abatement of this pollutant is of significant practical interest to improve our indoor air quality. HCHO can be removed from air by various methods such as adsorption, membrane separation, condensation, combustion or photocatalytic oxidation [1], however heterogeneous catalytic oxidation is the most promising way. This process completely oxidizes the organic pollutant into non-harmful molecules such as CO2 and H2O, with low energy consumption [1]. Supported noble metals have been proposed as efficient heterogeneous catalysts for HCHO oxidation at low temperature (b100 °C). Several catalysts have been developed such as Pt/TiO2 [2–4], Pd/TiO2 [5], Ag/TiO2 [6],

Au/TiO2 [7], Pt/Al2O3 [8], Ag/CeO2 [9] and Au/MnO2 [10]. Pt-based catalysts have been found to have the best catalytic activities with complete HCHO conversion at room temperature [11]. Nevertheless, the replacement of Platinum Group Metals (PGM) in catalytic formulations is required because noble metals are expensive and identified as critical raw materials by the European Union. Transition metal oxide based catalysts such as MnOx, CeOx, MnOx- CeO2 and CoOx [12–15] are efficient low-cost alternatives for HCHO catalytic oxidation. The pioneering work carried out by Sekine [16] demonstrated that manganese-based catalyst was the best transition metal oxide for HCHO oxidation. Manganese oxides have low volatility and toxicity, various crystal phases, variable valence states and low costs, making them attractive prospects in the field of heterogeneous catalytic oxidation. MnO2 has often been used for the catalytic oxidation of HCHO [13,17–21] but it is also efficient with other pollutant removal such as ethanol [22], ozone [23], toluene [24], NO [25] and dimethyl ether [26]. In the case of HCHO, the birnessite phase (δ-MnO2) has been found to be most efficient for low temperature catalytic oxidation [18,21] due to the presence of structural water between the birnessite layers, which adsorb HCHO and also replenish hydroxyl radicals, a powerful oxidant by reacting with adsorbed oxygen from the air ($O_2- + H_2O \rightarrow 2OH^*$). Also of utter importance for efficient catalytic oxidation, is the presence of manganese vacancies [20] or oxygen vacancies [23], which facilitate the cycling of oxygen species to and from the catalyst surface. Hollow sphere architecture is very interesting in that it has high surface area, low diffusion resistance and improved contact with the reactants due to the hollow space acting as a reservoir [27]. Hollow MnO2 spheres are generally synthesized by a hydrothermal templating method using silica (SiO2) spheres as a hard template or vesicles as soft template [27–29]. However, when SiO2 is used as template, a hydrothermal method at temperature higher than 140 °C for extended time (N40 h) is required, due to the low crystallisation rate of MnO2 from MnO4− precursor in aqueous solution ($4MnO4− + 2H_2O \rightarrow 4MnO2 + 4OH− + 3O_2$). Moreover the thin oxide wall

obtained (~15 nm) consists of MnO2 crystallites which are susceptible to breakage [30,31]. Alternatively, when organic templates are used, carbon residues remain in the MnO2 hollow spheres [30] that can potentially reduceMnO2 to Mn3O4 (which has relatively lower oxidizing potential). In most reported cases for the synthesis of hollow MnO2 spheres, the birnessite phase was obtained, showing a lack in versatility in those methods to obtain other phases. Therefore, a simple low temperature synthesis method that can: (1) coat a reasonable amount of MnO2 onto the template (to obtain a relatively thick wall and prevent breakage), (2) avoid any organic contamination, (3) provide high surface area and pore volume and (4) allow the production of different crystal phases, is required to produce MnO2 hollow spheres. A study by Jolivet's group [32] had demonstrated the versatility of the "one-pot" low temperature MnO4−/Mn2+ redox reaction at producing different MnO2 crystal polymorphs by controlling different reaction parameters such as acidity and reactant ratio. We herein utilize the MnO4−/Mn2+ reaction to report a new low temperature method for the synthesis of MnO2 hollow spheres by a controlled precipitation by redox (CPR) method, using SiO2 spheres as sacrificial templates. The MnO2 was coated by controlling the redox precipitation reaction of Mn2+ with MnO4- (according to the formal redox reaction given by Eq. (1)) at a temperature of 30 °C for 6 h, by a dropwise precursor addition method. This was followed by calcination of the core-shell SiO2@MnO2 and finally template removal by NaOH etching.

$$2KMnO4- + 3Mn(NO3)2 + 2H2O \rightarrow 5MnO2 + 4HNO3 + 2KNO3 \qquad (1)$$
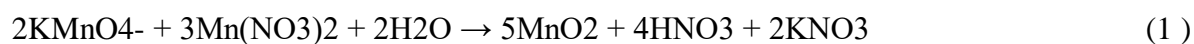
The aim was to achieve: high coating amount, high BET surface area and pore volume, relatively thick-walled spheres (due to high MnO2 loading), a relatively high oxidation potential as well as presence of oxygen vacancies and hierarchical porous structures from a simple low temperature aqueous method. Furthermore, the possibility of tuning different MnO2 phases for the hollow sphere shell from simple changes in the experimental protocols was evaluated. The catalysts were used for the low temperature catalytic oxidation of formaldehyde.

The performances of the synthesized samples were assessed according to a reference hollow sphere birnessite sample Bir(N), also synthesized by a low temperature method. The significance of this work lies in the development of a new cheap, facile and low temperature method (alternative to the lengthy and high temperature hydrothermal method) for the synthesis of MnO2 hollow spheres that can be utilized for various applications. As a proof of concept, the hollow spheres were successfully tested for the catalytic oxidation of formaldehyde at low to moderate temperatures.

2. Experimental

2.1. Materials

Tetraethylorthosilicate (TEOS, 98.0%), aqueous ammonia (28–30% solution), absolute ethanol (≥99.8%), potassium permanganate (KMnO4, ≥ 99.0%), manganese nitrate tetrahydrate (Mn(NO3)2·4H2O, ≥ 97.0%) and sodium hydroxide (NaOH, 98.0%) were purchased from Sigma-Aldrich and used as received without any further purification.

2.2. Synthesis of MnO2 hollow spheres

The general synthesis steps of the CPR method for the hollow MnO2 spheres included classical hard templating using SiO2 as templates, as simplified in Scheme 1. TheMnO2 shell was formed by low temperature CPR reaction whereby the Mn precursors were added dropwise. The SiO2@MnO2 core-shell sphere was then calcined followed by SiO2 template removal by NaOH etching, resulting in theMnO2 hollow shells. The SiO2 template was synthesized by a classical Stöber method (see SI for synthesis method) and had a diameter in the range 150–170 nm. In the naming convention for our samples, 'Mn' stands for MnO2, 'P' for permanganate Mn(VII) solution and 'N' for nitrate Mn(II) solution. The letter between the square brackets [] represents the solution that was added dropwise.
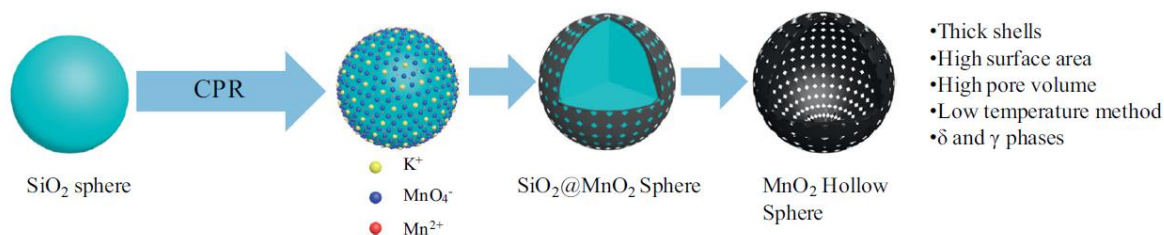
Scheme 1: Brief description of the hard templating method to synthesize MnO2 hollow spheres.

2.2.1. Synthesis of Mn[P]N

0.2 g of SiO2 spheres and 0.173 g of Mn(NO3)2·4H2Owere added to 20 ml DI water and the mixture was sonicated for 20 min. The suspension was then transferred to a magnetic stirrer and a solution of 0.073 g KMnO4 (in stoichiometric amount according to Reaction (1)) in 10 ml DI water was added dropwise at a rate of ~0.33ml min−1 under stirring. At the beginning, the mixture colour changed from white into light brown upon addition of KMnO4 and became purplish-brown upon addition of the last drop. The resulting mixture was allowed to react for 6 h at 30 °C after which the mixture had turned black. The initial light brown colour was a result of MnO2 nanocrystallites formation in the white suspension of SiO2 and Mn(II). As the CPR reaction proceeded, more MnO2 formed, coating the SiO2 template and turning the mixture black. The solid was collected by centrifugation, washed with DI water and oven-dried overnight at 70 °C. The dried SiO2@MnO2 solid was then calcined in a muffle furnace at 300 °C for 6 h (2 °C min−1 ramp). The SiO2 template was removed by stirring the SiO2@MnO2 in a 4 M NaOH solution at 50 °C for 4 h. Finally, the hollow spheres were collected after centrifugation, thorough washing with DI water (until the pH of the centrifugate was ~7) and drying overnight at 70 °C.

2.2.2. Synthesis of MnP[N]

The procedure for MnP[N] synthesis was similar to that for Mn[P]N, except that the KMnO4 was in the beaker mixed with the SiO2 spheres while the Mn(NO3)2·4H2O aqueous solution was added dropwise. Upon addition of the final drop of Mn(NO3)2·4H2O, the mixture was purplish-brown and after 6 h of reaction the mixture had turned black. The hollow spheres were obtained following the same experimental procedures as above.

2.2.3. Synthesis of Mn[P][N]

Here, both the Mn(NO3)2·4H2O and KMnO4 (each dissolved in 10 ml DI water in two separate beakers) were added to the SiO2 spheres dispersed in 10 ml DI water in another beaker. The mixture colour changed to light brown upon addition of the first drops to purplish brown after the final drops. At the end of the 6 h reaction, the mixture had turned black. The hollow spheres were obtained following the same experimental procedures as above.

2.3. Characterization

X-ray diffraction (XRD) patterns were recorded on a Bruker X-ray diffractometer at room temperature with Cu Kα radiation ($\lambda = 1.5418$ Å). The data sets were collected in the 10°−80° range with a step size of 0.04° and an integration time of 2 s. Raman spectra were recorded on a XY800 Raman Dilor spectrometer equipped with an optical multichannel detector and set in macro-configuration mode. Bulk analysis was performed on a heaped amount of sample placed in front of the laser so as to obtain an average spectrum from a large area of the sample. A 647.1 nm laser light was used at low excitation power of 10mW. To have a high signal to noise ratio, each Raman spectrum was taken as an average of 4 successive scans with an accumulation time of 300 s. The sample morphology was characterized by Transmission electron microscope (TEM) and high-resolution transmission electron microscope (HRTEM) using a Tecnai 200 kV with LaB6 filament. N2 adsorption desorption isotherms were measured at liquid nitrogen temperature, using a gas adsorption analyser (TriStar II 3020). Total pore volume was

determined at P/P0=0.99 and the BET method was used to calculate the specific surface areas. The samples were degassed at 150 °C for few hours under vacuum before measurement. X-ray photoelectron spectroscopy (XPS) were conducted using an AXIS Ultra DLD Kratos spectrometer equipped with a monochromatized aluminium source (Al Kα = 1486.7 eV) and charge compensation gun. All binding energies were referenced to the C 1s core level at 285 eV. Simulation of the experimental photopeaks was carried out using a mixed Gaussian/Lorentzian peak fit procedure according to the CasaXPS software. Reducibility of the catalyst was measured by hydrogen temperature programmed reduction (H2-TPR) technique. ~20 mg of the sample was placed in a quartz reactor connected to a TPR apparatus (Micromeritics model AutoChemII). The sample was heated in air at 150 °C for 0.5 h to remove adsorbed water and then cooled down to close to room temperature. Then the reactor was heated from 40 °C to 600 °C with a heating rate of 10 °C min−1 in a gas mixture (5% H2+95% Ar, 50 ml min−1). The amount of H2 consumption was analysed by a thermal conductivity detector (TCD).

2.4. Catalytic oxidation tests

The catalytic oxidation of formaldehyde was performed in a fixed-bed reactor (internal diameter=10mm) loaded with the catalyst (200mg). Before each light-off test, the catalyst was pretreated for 1 h at ~150 °C under O2/N2 flow (20 Vol%; total flow rate of 100 ml min−1) to remove water and surface impurities. Gaseous formaldehyde was generated from solid para-formaldehyde in a permeation tube placed in a permeation chamber (Dynacalibrator, VICI Metronics Inc.). By adjusting the gas carrier flow (20% O2/N2) and the chamber temperature, a stable formaldehyde concentration was produced. The inlet concentration of formaldehyde was fixed at 100 ppmv, and the total flow rate was 100 ml min−1 resulting in a GHSV of 30,000 h−1. The reactor temperature was decreased from150 °C to ~30 °C at a ramp of−0.2 °Cmin−1.

In these decreasing temperature tests, only catalytic oxidation occurred initially and adsorption on the material started as the temperature reached around 120 °C.

Stability tests were performed with 200 mg of each sample. The reactor temperature was set at the corresponding T50 of each sample. No pre-treatment of the catalyst was performed before the test to investigate the effect of adsorbed water on formaldehyde oxidation. The inlet concentration of formaldehyde was fixed at 100 ppmv in dry air, and the total flowrate was 100ml min−1 resulting in a GHSV of 30,000 h−1. The effluent gases were analysed online with a Varian CP-4900 Micro-GC equipped with a thermal conductivity detector. Formaldehyde conversion was evaluated from either the formaldehyde or carbon dioxide concentration by systematically calculating the carbon balance to ensure that formaldehyde consumption produced carbon dioxide (no partial oxidation and no adsorption). The formaldehyde conversion (XHCHO, %) was determined using the following equation:

XHCHO (%) = ([CO2]/ [HCHO]ini)x100

with [CO2] being the concentration of CO2 at time t and [HCHO]ini being the inlet formaldehyde concentration.

3. Results and discussion

3.1. Characterization

The crystal structure of Mn[P]N, MnP[N], Mn[P][N] and of the reference sample Bir(N) (see Bir(N) synthesis in SI) was determined by XRD and the patterns are presented in Fig. 1. The weak and broad diffraction peaks for all samples indicate low crystallinity and/or presence of nanocrystallites. Mn[P]N has distinct peaks at 23.4°, 37.2°, 42.5°, 57° and 65.7°, which can be assigned to reflection of planes (120), (131), (300), (160) and (421) of nsutite type MnO2 (γ-

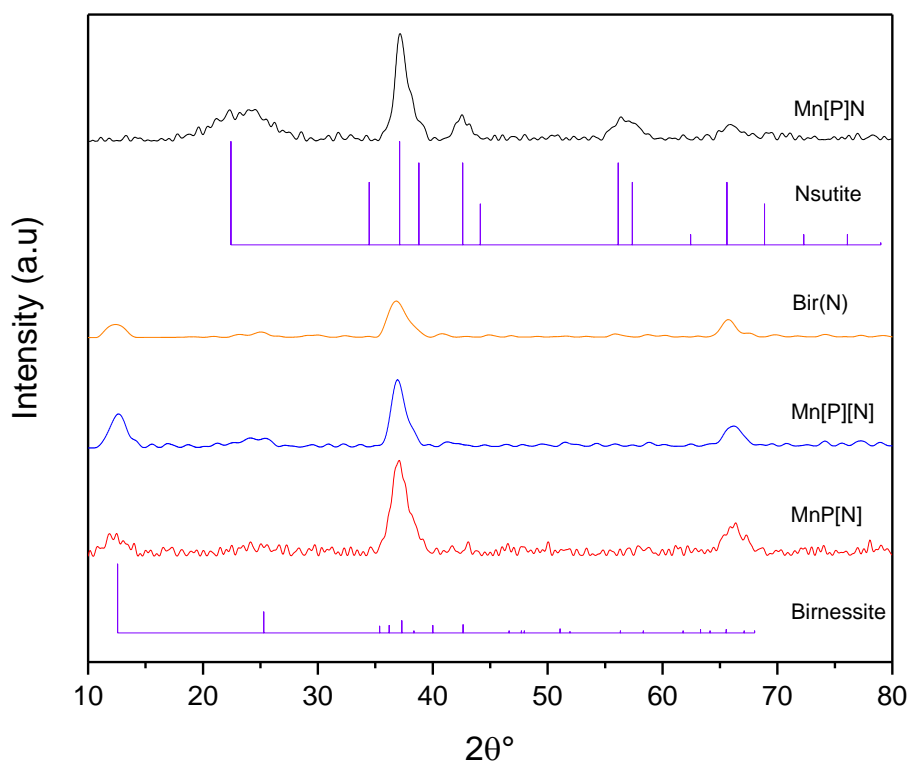MnO2, JCPDS 14-0644, crystal system: orthorhombic, lattice parameters: $6.36 \times 10.15 \times 4.09$ Å).

Figure 1: XRD patterns for Mn[P]N, MnP[N], Mn[P][N] and Bir(N)

Nsutite generally consists of an intergrowth of pyrolusite blocks within a ramsdellite matrix [33]. The γ-MnO2 phase was also obtained in a previous study by Wang et al. who used a similar synthesis method to load MnO2 flakes onto activated carbon fibers, followed by calcination at 200 °C under N2 [34]. Furthermore, Jolivet and co-workers [32] showed that the γ-MnO2 phase could be formed at low temperature and low pH for the MnO4−/Mn2+ system when theMnO4−:Mn2+ ratio was 2:30, i.e., when the Mn2+ concentration was in high excess. This was the case for the synthesis of Mn[P]N since the MnO4− was added dropwise to a suspension containing the Mn2+. However, the γ-MnO2 phase is metastable and can transform into the α-MnO2 phase, but studies [32,35] have shown that low reaction temperature (≤60 °C) and short reaction time for the MnO4−/Mn2+ system can stabilize the γ-MnO2 phase.

Calcination is another parameter that can affect the γ-MnO2 phase. Fu et al [36] found that γ-MnO2 changed to β-MnO2 and Mn2O3 following calcinations at 350 °C and 460 °C in air, respectively. Therefore, it can be said that the low reaction temperature (30 °C), relatively short reaction time (6 h) and moderate calcination temperature of 300 °C used in the CPR method effectively stabilized the γ-MnO2 phase for Mn[P]N. On the other hand, the reference sample Bir(N), MnP[N] and Mn[P][N] have peaks located at around 12.5°, 25.3°, 37° and 66.2° corresponding to reflection of planes (001), (002), (-111) and (005) typical to K-birnessite type MnO2 (δ-MnO2, JCPDS 80–1098, crystal system: hexagonal, lattice parameters: 5.149 × 2.843 × 7.176 Å) [20,37–40]. Birnessite consists of sheets of MnO6 octahedra with randomly distributed water molecules and cations such as Na+ and K+ between the interlayers. Jolivet and co-workers [32] also reported the formation of the δ-MnO2 phase at $4 \leq pHf \leq 12$ and MnO4−:Mn2+ ratios of 2:3 (stoichiometric) and 20:3 (MnO4− in excess). Again these were the cases respectively, for the synthesis of Mn[P][N] whereby both Mn precursors were added dropwise in stoichiometric amounts and for MnP[N] whereby the Mn2+ was added dropwise to a suspension containing the MnO4−. The interlayer spacing represented by the peak at around 12.5° was calculated to be 7.08 Å from the Bragg diffraction eq. (2d sinθ=λ). This value is lower than the reported JCPDS value of 7.176 Å, probably due to the presence of Na+ ions that were incorporated within the interlayers during the etching process. Na+ ions (1.02 Å) are smaller than K+ ions (1.38 Å) and may be the cause for the reduction in interlayer distance. The XRD results therefore show that two different MnO2 polymorphs could be easily obtained by simple modifications in the precursor addition. Previous studies have demonstrated that the K+ concentration in solution can affect the crystal phase of the initial MnO2 seeds in solution [41,42]. The K+ concentration needs to be at a high enough concentration during crystal growth so as to intercalate in-between the MnO2 sheets and eventually stabilize the δ-MnO2 phase. If not enough K+ is present, the layered structure collapses into a tunnel structure, which in our

case is the 1×1 and 2×1 tunnel structure of γ-MnO2. Raman scattering analysis is a very useful technique for the study of the local structure of MnO2, especially if the samples are of low crystallinity. Macro-Raman spectrometry was carried out on the three synthesized samples so as to determine their bulk composition. Macro-Raman studies have been performed before to successfully differentiate between different MnO2 polymorphs such as α-, β-, γ-, and δ-MnO2 [43–45]. In this study, we utilize a 647.1 nm laser light as it was found to give intense and best resolution of Raman peaks for manganese oxides [46]. A laser power of 10 mW and macro-hole were chosen to allow for a low power density irradiating the sample, therefore preventing the phase transformation of MnO2 into Mn2O3 and Mn3O4 [43–45]. Fig. 2 shows the Raman spectra of the synthesized MnO2 samples. Mn[P][N] and MnP[N] are similar, with major peaks at ~574 cm−1 and ~642 cm−1 and smaller peaks at ~514 cm−1 and ~730 cm−1. For Mn[P]N, major peaks are observed at ~573 cm−1 and ~646 cm−1 and minor peaks at ~519 cm−1 and ~746 cm−1, while a shoulder is also found at ~561 cm−1. It is to be noted that Mn3O4 (characterized by an intense peak at ~650 cm−1) and Mn2O3 (characterized by a peak of medium intensity at ~680 cm−1) were not present in the samples [46]. Generally, manganese oxides have three major regions on the Raman spectra situated at 200–450, 450–550 and 550–750 cm−1 which correspond to spectral domains where the skeletal vibrations, the deformation modes of the metal-oxygen chain of Mn\\O\\Mn in the MnO2 octahedral lattice and the stretching modes of the Mn\\O bonds inMnO6 octahedra occur, respectively [47]. In particular, for birnessite MnO2 three major features occur at around $υ1 = 500–510$ cm−1, $υ2 = 575–585$ cm−1 and $υ3 = 625–650$ cm−1, which are attributed to the (Mn\\O\\Mn) flexural vibration of MnO6 groups, the stretching vibration $υ 2(Mn\\O)$ in the basal plane of MnO6 sheets and the symmetric stretching vibration $υ3(Mn\\O)$ of MnO6 groups, respectively [43].
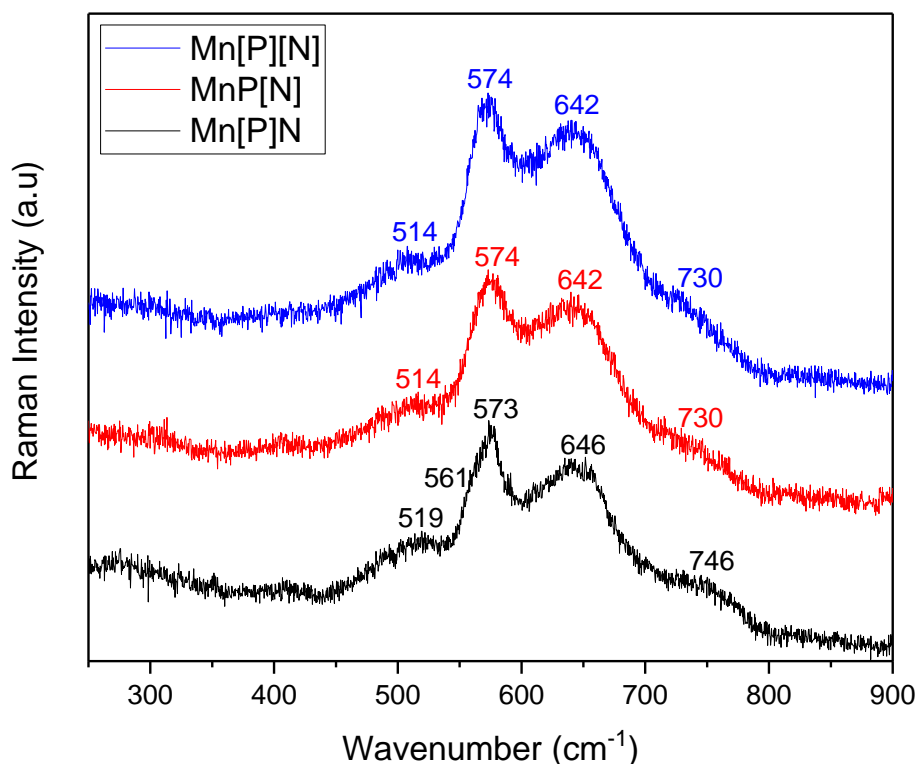
Figure 2: Raman spectra of Mn[P]N, MnP[N] and Mn[P][N]

The Raman spectra for Mn[P][N] and MnP[N] are similar in terms of shape and peak positions to previously reported birnessite MnO_2 Raman spectra [43]. The major peaks positions for Mn[P]N also seem to point towards birnessite MnO_2. However, there is an increase in the vibrational frequency of $\upsilon 3$ at 646 cm−1 for Mn[P]N compared to 642 cm−1 for the other two samples. This increase in the stretching vibration of the Mn\\O bond may be attributed to a decrease in the number of edges shared by each MnO_6 octahedron [43]. This could also explain the increase in vibrational frequency to 746 cm−1 for Mn[P]N compared to the peak at 730 cm−1 for Mn[P][N] and MnP[N]. Nsutite which is a mixture of ramsdellite (4 edges shared) and pyrolusite (2 edges shared) has fewer edges shared per MnO_6 octahedron than the more compact layered birnessite MnO_2. It has been reported that the characteristic Raman peaks for γ-MnO_2 lie in the range 500–700 cm−1 [44], which could also explain the appearance of the

shoulder at ~561 cm−1 in Mn[P]N. The Raman spectrum for nsutite type MnO2 has been characterized in detail previously [44,48]. Indeed the observed major and minor peaks for Mn[P]N closely match reported spectrum shape [48] (especially with the relatively sharp peak observed at ~573 cm−1, compared to the other two birnessite spectra) as well as peak positions for nsutite MnO2 with approximately 34% pyrolusite content [44]. The similarity between the Raman shapes for Mn[P]N compared to Mn[P][N] and MnP[N] may be because during synthesis of Mn[P]N, birnessite sheets initially formed but then collapsed into tunnel structures with time, due to insufficient K+ concentration present in the mixture at any time to sustain the layered structure. The tunnel structure has fewer edges shared per MnO6 octahedron than layered birnessite MnO2, causing an increase in the symmetric stretching vibration v 2(Mn\\O) of MnO6 groups, explaining the shift in Raman wavenumbers to higher frequencies and possibly the appearance of the shoulder (due to an additional peak) at ~561 cm−1 in Mn[P]N.

Fig. 3a, b and c show the TEM images of Mn[P]N, MnP[N] and Mn[P][N], respectively. Fig. 3a shows aggregated hollow spheres with the shells consisting of flaky structures for Mn[P]N. The flaky structures may have been obtained as a result of the collapse of sheet like birnessite structures initially formed during the CPR reaction, due to the lack of K+ ions to sustain the birnessite sheet-like morphology. On the other hand, Fig. 3b and c show sheet-like structures wrapped into hollow spheres for MnP[N] and Mn[P][N], respectively. As a matter of fact, thin sheet like morphology has been commonly reported for birnessite type MnO2 [38–40]. The hollow sphere structure for all samples can be more clearly seen on the magnified TEM images (see insets in top right corner of Fig. 3a, b and c). The hollow space inside the spheres correspond to the diameter of the SiO2 spheres template (150–170 nm). The diameter and shell thickness of the hollow spheres were all in the range 230–300 nm and 23–55 nm, respectively. The lattice parameters for the hollow spheres were determined via HRTEM (Fig. S1). For Mn[P]N, values of 0.4 nm and 0.53 nm were found. The former value could be indexed to (120)

reflection ofγ-MnO2 [26] while the value of 0.53 nm may correspond to collapsed interlayer spacing of δ-MnO2 structure due to the vacuum of the electron microscope [49]. MnP[N] has lattice parameters of 0.44 nm and 0.7 nm which could be indexed to the (100) plane of ramsdellite-type MnO2 [50] and the interlayer spacing of δ-MnO2, respectively [49].
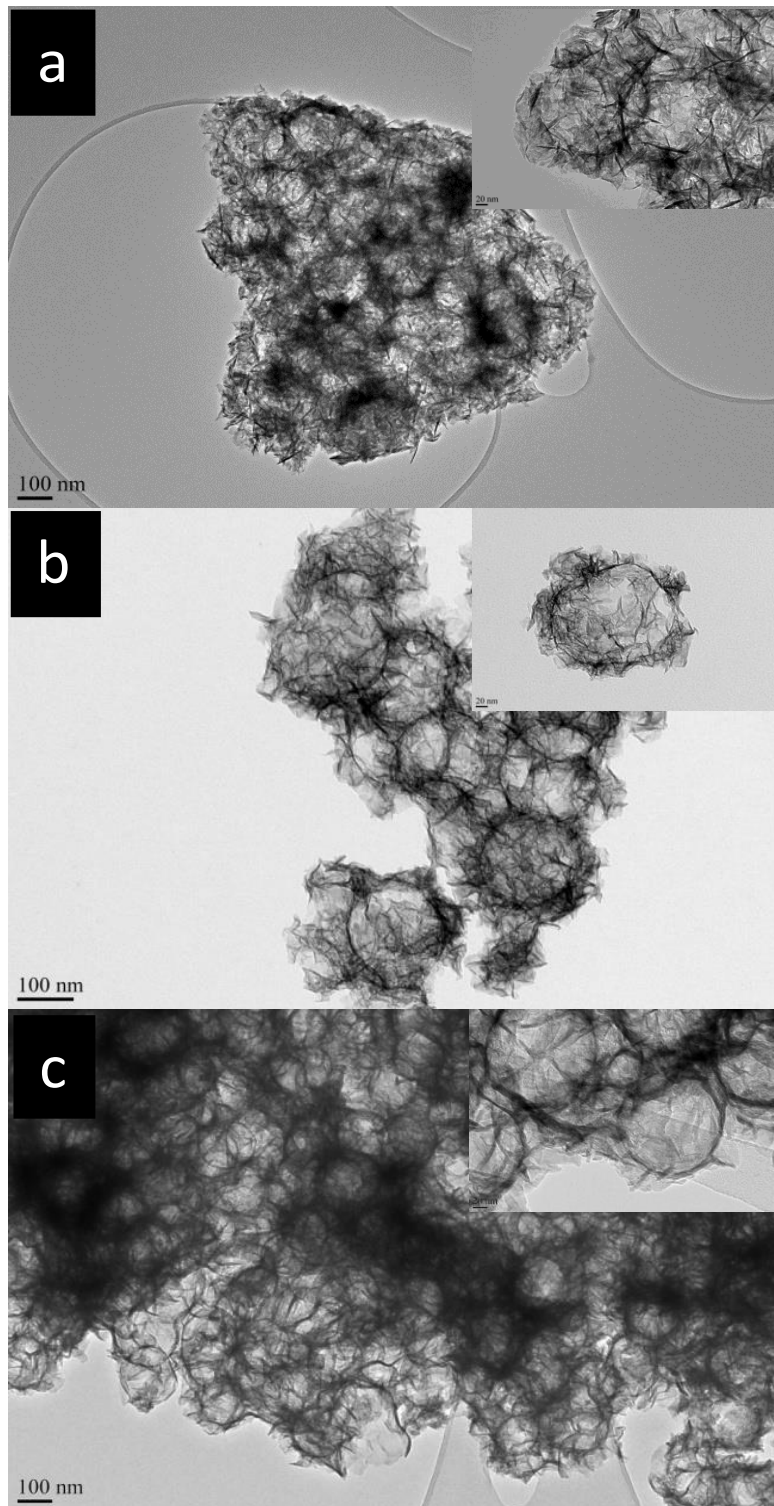
Figure 3: TEM images of a) Mn[P]N, b) MnP[N] and c) Mn[P][N]

Finally, for Mn[P][N], values of 0.7 nm and 0.5 nm were indexed to interlayer spacing of δ-MnO2 [49] and possibly the result of collapsed interlayer spacing due to the vacuum of the

electron microscope [49], respectively. From these results, it appears that Mn[P]N and MnP[N] were mixed phases. However, since the evidence of the mixed phase was apparent mainly via HRTEM and not XRD, it can be said that the secondary phase was present in very small fraction. From the information obtained by XRD, Raman, TEM and HRTEM, the steps and mechanism involved in the hollow spheres' formation could be deduced. The steps involved by the CPR method is briefly illustrated in Scheme 1. A classical templating synthetic method was employed by using silica spheres as hard templates. MnO_2 was coated onto the SiO_2 by the CPR method to obtainMnO2@SiO2 core-shell particles. Using MnP[N] synthesis as an example, the Mn^{2+} precursor was added drop by drop in a mixture containing SiO_2 spheres and $KMnO_4$ to control the precipitation rate of MnO_2 on the SiO_2 spheres. The SiO2@MnO2 core-shell particles were then calcined at 300 °C to crystallize the MnO_2. Finally, the SiO_2 template was removed by treatment in hot concentrated NaOH solution to obtain MnP[N] hollow spheres. The formation mechanism of birnessite MnP[N] can be described as follows. Initially the mixture contained SiO_2 spheres and $KMnO_4$. The K^+ ions get attracted to the negative oxygen groups on the SiO_2 sphere's surface (silanol Si-O-H groups) resulting in a high concentration of K^+ ions around the SiO_2 spheres. With the controlled addition of Mn^{2+}, the cations also anchored to the Si-O-H groups and MnO_2 units were formed by redox reaction with MnO_4^-. The high concentration of K^+ ions at the vicinity of the spheres' surface favored and stabilized the formation of birnessite sheets which curled and crumpled around the SiO_2 spheres. Finally, upon NaOH etching of the SiO2@ MnO2 core-shell spheres for removal of the template, hydrated Na^+ species penetrated and settled in the interlayer for charge balance due to presence of Mn^{3+}, resulting in layered birnessite MnO_2 hollow spheres. If the K^+ concentration was too low at any time, the birnessite sheets could not be sustained and instead collapsed into the tunneled structure γ-MnO_2 phase as with Mn[P]N, however a minor amount of δ-MnO_2 may be formed towards the end of the reaction when all the $KMnO_4$ had been

added, since at that point, enough K+ ions were present in the mixture to sustain the layered birnessite structure. Conversely, for MnP[N] a minor amount of ramsdellite could have formed towards the end of the reaction (as seen from the previous HRTEM results), when the amount of K+ ions present in the mixture was not enough to sustain the birnessite layered structure. The CPR method used in this work is advantageous in that it is a facile low temperature method for the synthesis of high surface area hollow particles and allows relatively high coating amount (0.5 g MnO_2 per g SiO_2) and therefore thick-walled shells, as opposed to classical high temperature hydrothermal method using SiO_2 as templates. Moreover, different MnO_2 phases could be obtained by simple changes in the precursor addition protocols.

N_2 adsorption isotherms for the three synthesized hollow spheres samples are presented in Fig. 4. From the figure, all samples exhibited Type II behavior with Type H3 hysteresis loop in the relative pressure (P/P0) range 0.42–1.0, suggesting the existence of slit-shaped mesopores with non-uniform sizes or shapes, probably due to aggregation of nanoparticles [26,39,51,52].
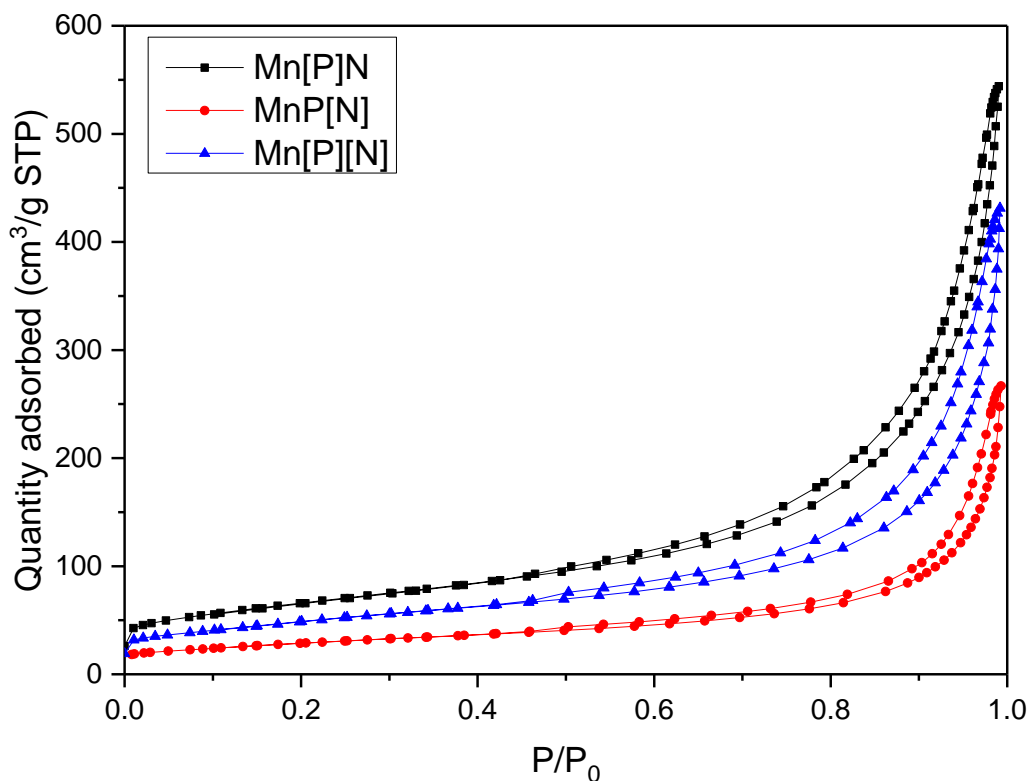
Figure 4: N$_2$ adsorption isotherms for Mn[P]N, MnP[N] and Mn[P][N]

A rapid increase in N2 adsorption in the low-pressure region (up to P/P0 ~ 0.025) was due to the presence of micropores formed by tunnel structures in Mn[P]N and interlayer spacing in MnP[N] and Mn[P][N]. This is followed by a quasi-linear increase up to P/P0=0.8 which accounts for the filling of mesopores after which a sharp increase in the range 0.8–1.0 is observed, which corresponds to larger mesopores and macropores filling inside interparticle voids and hollow cavity of the spheres, respectively. Therefore, the hollow spheres samples possessed hierarchical pore size distribution with micropores, mesopores and macropores. The BET surface areas and total pore volumes (Vt) of the samples are presented in Table 1. The BET surface areas of Mn[P]N, MnP[N] and Mn[P][N] were 236 m2 g−1, 104 m2 g−1 and 176 m2 g−1, respectively while the total pore volumes were 0.84 cm3 g−1, 0.41 cm3 g−1 and 0.67 cm3 g−1, respectively. Although MnP[N] and Mn[P][N] have similar morphologies, their BET

surface areas and Vt largely differ. From XPS results (presented next), we found that the calculated amount of adsorbed water in MnP[N] was much higher than in Mn[P][N] (21.6% versus 8.4%). It may be possible that some structural water remained strongly bound between the birnessite sheets of MnP[N] after degassing, prior to N2 physisorption studies. This could block the entrance of N2 probe molecules, resulting in a lower estimation of BET surface area and Vt.

Table 1: Summary of results from N_2 adsorption, XPS analysis, H_2-TPR and corresponding T_{50} and T_{90} for Mn[P]N, MnP[N] and Mn[P][N]

| Sample | N_2 adsorption | | XPS analysis | | | | | | TPR | HCHO oxidation | |
	BET ($m^2 g^{-1}$)	V_t ($cm^3 g^{-1}$)	Mn^{4+}/Mn^{3+}	K/Mn^{3+}	$(K+Na)/Mn^{3+}$	O2/O1	AOS	%MnO_x	AOS*	T_{50} (°C)	T_{90} (°C)
Mn[P]N	236	0.84	3.46	0.06	1.26	0.44	3.68	92.6	3.31	75.6	99.7
MnP[N]	104	0.41	2.72	0.05	1.33	0.65	3.48	90.7	3.58	80.3	109.2
Mn[P][N]	176	0.67	2.15	0.12	0.86	0.65	3.45	92.3	3.44	84.6	108.1

The XPS survey spectra show that Mn, O, K and Na were present in Mn[P]N, MnP[N] and Mn[P][N] (Fig. S2). The high resolution XPS spectra for Mn, O and K for sample Mn[P]N is shown in Fig. 5 while the corresponding spectra for MnP[N] and Mn[P][N] are presented in Fig. S3 and Fig. S4, respectively. The Mn2p spectrum for all samples had 2 peaks located at ~654 eV and ~642.1 eV, which were attributed to Mn2p1/2 and Mn2p3/2, respectively. The spin-energy separation between these 2 peaks, ΔEp was ~11.9 eV for all samples, indicative of the presence of mostly Mn4+ [53,54]. To determine the Mn species in the samples, the more intense 2p3/2 signal was considered for decomposition. Mn4+ correlated with 6 decomposed peaks (Mn1 – Mn6) [55]. Moreover, the small peak at low B.E. of 641.2 eV was attributed to Mn3+ [55–57]. The surface atomic percentage distribution of O, Mn, K and Na functional groups as well as their binding energies (B.E (eV)) are presented in Table S1. The O1s spectra could be decomposed into 3 types of oxygen for all samples, namely O1 (~529.8 eV), O2 (~531.3–531.9 eV) and O3 (532.6–533.6 eV) which were attributed to lattice oxygen

[20,21,26,54,58–60], surface adsorbed oxygen (such as O2−, O− and terminal OH group) [20,21,61] and adsorbed/interlayer water [20,54,61,62], respectively. The O2 binding energy for MnP[N] (531.9 eV) was higher than Mn[P]N (531.3 eV) and Mn[P][N] (531.5 eV), possibly due to a higher concentration of strongly bound surface oxygen species in MnP[N]. On the other hand, the O3 binding energy of Mn[P]N (532.6 eV) was lower than that of MnP[N] (533.5 eV) and Mn[P][N] (533.6 eV), respectively because interlayer water is strongly bound via their oxygen atoms to the interlayer cations in birnessite-type MnO2 and by hydrogen bonds to hydroxyl groups. The K peaks lie in the vicinity of the C1s region and could be decomposed into 2 peaks K1 (~292 eV) and K2 (~295 eV). The atomic% composition of the elements in each sample, calculated by CasaXPS is presented in Table S2.
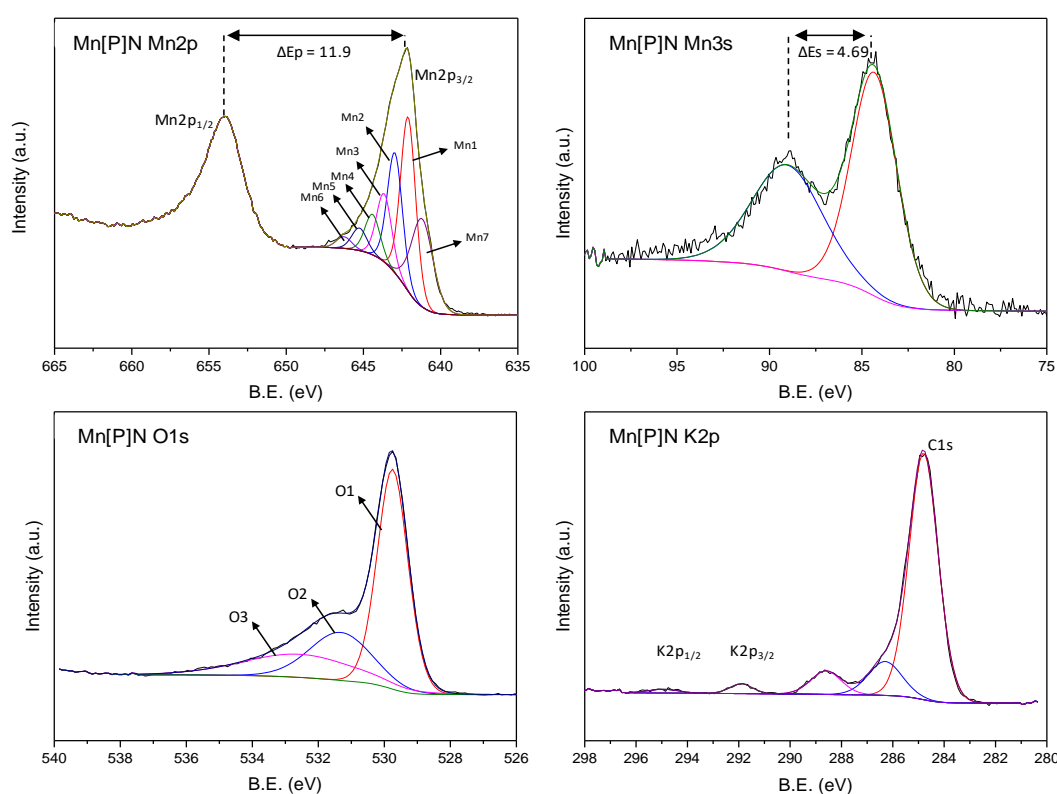

Figure 5 : Decomposed high resolution XPS spectra of Mn2p, Mn3s, O1s and K2p for sample Mn[P]N

Table 1 shows pertinent information from XPS analysis regarding the ratios of surface species present in the samples. Mn[P]N has the highest ratio of Mn^{4+}/Mn^{3+}, followed by MnP[N] and finally Mn[P] [N]. Mn^{4+}/Mn^{3+} ratios within the same range have previously been reported for γ-MnO2 [21] and δ-MnO2 [40]. The K/Mn^{3+} ratio for Mn[P] [N] is at least twice as much as with Mn[P]N and MnP[N], respectively. This is most likely due to the controlled dropwise addition of both Mn precursors during the synthesis of Mn[P][N], which allowed for a more homogeneous distribution of K within the sample during the formation of MnO2. To balance the charge in MnO2 due to the presence of Mn^{3+}, the ratio K/Mn^{3+} should be 1. However, this is not the case as seen in Table 1. Nevertheless, after NaOH etching, the ratio $(K+Na)/Mn^{3+}$ increased to around 1 for all the hollow sphere samples which satisfied the charge balancing conditions. The ratio O2/O1 is a measure of the oxygen species mobility on the surface of the samples. Surface oxygen species have higher mobility than lattice oxygen and higher surface oxygen concentration usually leads to better catalytic performance [26]. In that respect, MnP[N] and Mn[P][N] have the highest oxygen species mobility with a ratio of 0.65 while Mn[P]N, the lowest with 0.44. The oxygen species concentration is related to the oxygen vacancies present in the samples, which in turn is proportional to the amount of Mn^{3+}.

The average oxidation state (AOS) of the MnO2 samples can be calculated from the magnitude of the 3 s multiplet splitting (ΔEs) via the equation: $AOS = 8.956–1.126\Delta Es$ (eV) [64]. The AOS of the samples are also presented in Table 1. Mn[P]N has the highest AOS of 3.68 followed by MnP[N] and then Mn[P][N] with 3.48 and 3.45, respectively. The AOS is related to the oxidizing potential of the catalysts; the higher the AOS, the better the oxidizing capacity. Finally, from the atomic% data of the elements from Table S2 and the AOS for each sample, the wt% of MnOx in the sample was estimated and shown in Table 1. For catalytic oxidation, an efficient catalyst requires a high oxidizing power as well as high oxygen mobility (oxygen vacancies). However, high oxygen vacancies mean higher Mn^{3+} concentration and a resulting

reduced oxidizing capacity. Therefore, a compromise needs to be attained between both characteristics to result in an efficient catalyst.

The reducibility of the MnO2 samples was investigated by H2-TPR and the results are shown in Fig. 6. The reduction of Mn[P]N, MnP[N] and Mn[P][N] occurred in 2 distinct steps: a low temperature reduction (LTR) step between ~150 °C and ~325 °C and a high temperature reduction (HTR) step between ~325 °C and ~480 °C. The occurrence of a third small peak centered at 442 °C and 415 °C for MnP[N] and Mn[P][N], respectively may be due to minor quantity of different MnO2 phases (having different reducibilities) present in the samples [64]. Moreover, for samples Mn[P]N, MnP[N] and Mn[P][N] the onset of reduction starts at a temperature of ~130 °C, which is due to the presence of surface oxygen species on the catalysts' surfaces.
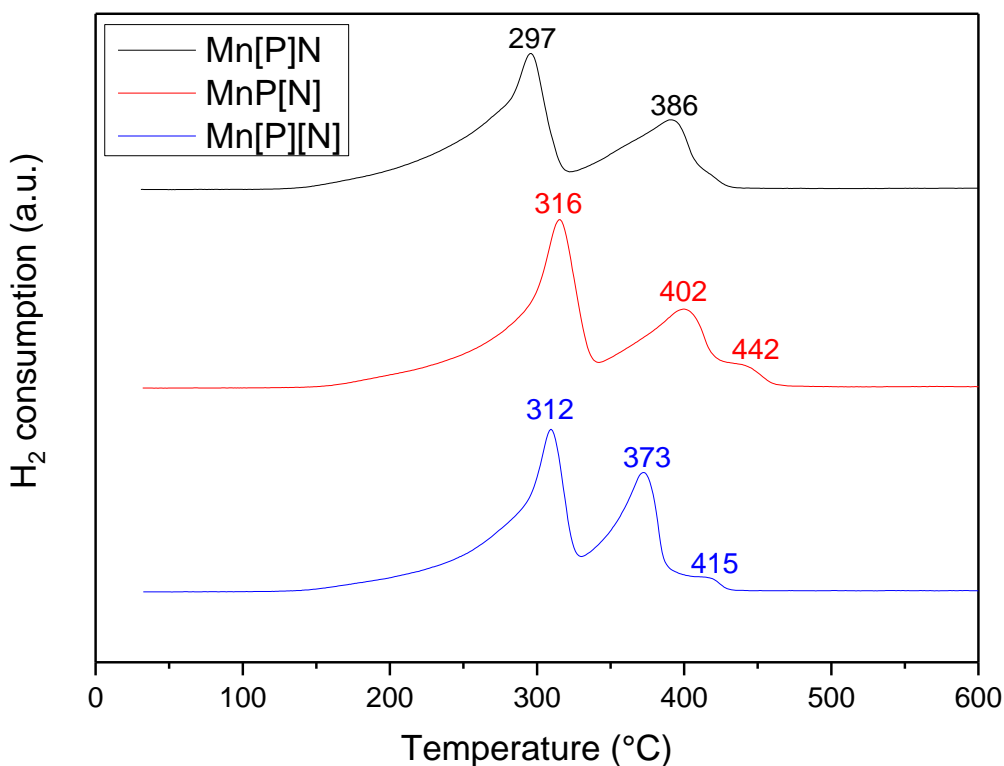
Figure 6 : H$_2$-TPR results for Mn[P]N, MnP[N] and Mn[P][N]

The amount of H2 consumed for each sample is given in Table S3, from which the AOS was calculated and presented in Table 1. A good agreement is found between the AOS values (<3% difference) calculated by XPS and H2-TPR for MnP[N] and Mn[P][N]. However, for Mn[P]N, a relatively larger 10% difference is found, which could be due to some non-homogeneity in the bulk of the sample. The ratio of the H2 consumption between the 2 reduction regimes (LTR/HTR) was calculated and compared with the theoretical H2 consumption ratio ((LTR/HTR)theo) by considering the reduction pathway to be MnOx → Mn3O4 for the first step (LTR) and Mn3O4 → MnO for the second step (HTR). The results are shown in Table S3. The LTR/HTR values for MnP[N] and Mn[P][N] are quite close to the theoretical values. However, LTR/HTR for Mn[P]N is 1.7 compared to a theoretical ratio of 1, meaning that 27%

of the Mn3O4 already converted to MnO in the LTR regime. It can therefore be deduced that Mn[P]N has the highest reducibility followed by Mn[P][N] and MnP[N]. In these cases, the reducibilities of the catalysts are closely correlated with their BET surface areas.

Table 2: Summary of synthesis methods, physical characteristics and applications of MnO_2 hollow spheres as obtained from literature

* maximum reported value, NR – not reported

| Sample name | Synthesis | | Physical characteristics | | | Application | Ref |
	Method	Template	Phase	BET S.A ($m^2 g^{-1}$)	Pore volume ($cm^3 g^{-1}$)		
Single-shelled MnO_2	Anion-adsorption hydrothermal	Carbonaceous microspheres	α	30	0.1	Pseudocapacitors	[29]
C/MnO_2 composite	Hydrothermal	N-doped hollow carbon spheres	δ	158	0.3		
MnO_2 HS	Hydrothermal	SiO_2 spheres	δ	119	0.3	Supercapacitors	[30]
α-MnO_2	Hydrothermal	None	α	109*	NR	Pseudocapacitors	[66]
Hollow MnO_2 sphere	Hydrothermal	SiO_2 spheres	δ	253	NR	Supercapacitors	[31]
Bir(N)	Emulsion	Soft (O/W interface)	δ	72	0.2	HCHO oxidation	[67]
Mn[P]N			γ	236	0.8		
MnP[N]	Low temperature CPR		δ	104	0.4		This work
Mn[P][N]		SiO_2 spheres	δ	176	0.7	HCHO oxidation	

The physical characteristics of our synthesized hollow spheres were compared to published data, and presented in Table 2. It can be noted that our synthesized spheres possess among the highest BET surface areas and pore volumes reported. Moreover, the MnO2 phases reported in the literature were of the α or δ type, while we successfully produced γ-MnO2 from our low temperature CPR method. Furthermore, MnO2 hollow structures have predominantly been used for energy storage applications, and we expect MnO2 hollow spheres synthesized from the low temperature CPR method to demonstrate interesting performances as well.

3.2. Catalytic performance

The performances of the hollow spheres samples were tested for formaldehyde complete catalytic oxidation into CO2 and H2O via dynamic light-off experiments, with the results shown in Fig. 7a. The T50 and T90 (corresponding temperatures for 50% and 90% of complete

oxidation respectively) are presented in Table 1, for all the samples. The T50 are 75.6 °C, 80.3 °C and 84.6 °C while the T90 are 99.7 °C, 109.2 °C and 108.1 °C for Mn[P]N, MnP[N] and Mn[P][N], respectively. The samples synthesized in this work largely outperformed the reference mesoporous hollow spheres sample Bir(N), which could oxidize only 34% of formaldehyde at 100 °C (Fig. 7a), despite its high surface area of 128 m2 g−1 and pore volume of 0.48 cm3 g−1 (see Fig. S5 for N2 adsorption isotherm of Bir(N)). Therefore, sample Mn[P]N has the lowest T50 and T90 of all the samples while MnP[N] and Mn[P][N] perform rather similarly.
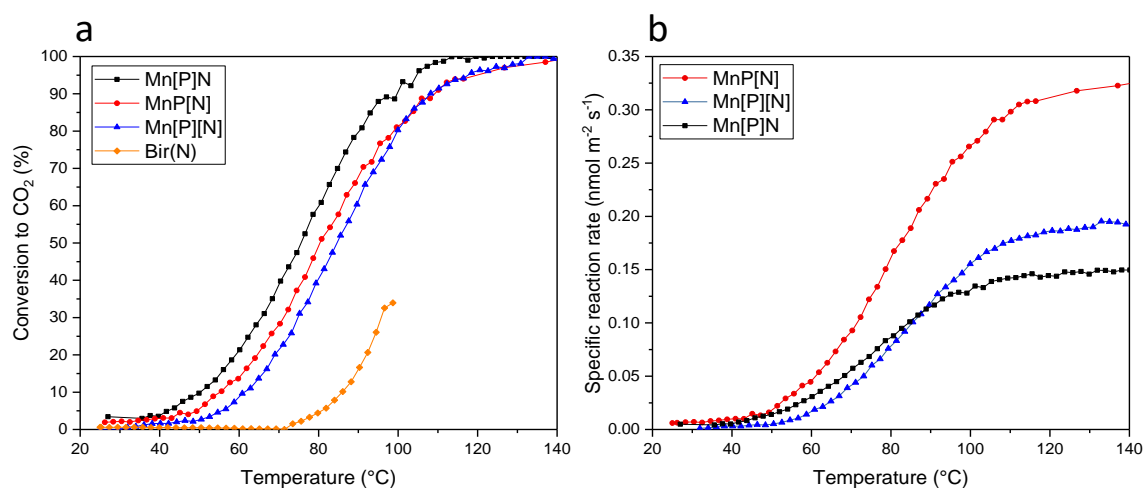

Figure 7: a) Light-off curves for Mn[P]N, MnP[N], Mn[P][N] and Bir(N), b) specific reaction rate for Mn[P]N, MnP[N] and Mn[P][N]

The best catalytic oxidation performance of Mn[P]N may be due to its highest surface area, out of all the samples. However, for the remaining birnessite MnO2 samples, the slightly better performance of MnP[N] might be due to its higher bulk AOS of 3.58 compared to 3.44 for Mn[P][N], despite the latter's higher surface area. The MnO2 hollow spheres synthesized in this work outperform other birnessite MnO2 found in the literature, for reactions carried out under dry conditions (Table S4). We also point that furthermore, some of the studies reported HCHO conversion in terms of HCHO balance (which accounts for conversion into CO2 and HCHO adsorption onto the catalyst) instead of complete conversion into CO2 as in this study. Since the BET surface areas of the synthesized samples largely differ from each other, the specific

reaction rate (per unit surface area of the samples, nmol m−2 s−1) was calculated to compare their catalytic efficiencies (Fig. 7b). It can be seen that MnP[N] has by far the highest specific reaction rate over the whole temperature range. Of the remaining samples, Mn[P][N] has higher specific reaction rate beyond 90 °C while below that temperature, Mn[P]N performed slightly better. The results mean that sample MnP[N] has the highest number of active sites per unit surface area, followed by Mn[P][N]. On the other hand, sample Mn[P]N despite its largest surface area, has the lowest number of active sites per unit area. The results are in accordance with the bulk AOS of the samples according to TPR (Table 1), whereby the AOS are in the order MnP[N] N Mn[P][N] N Mn[P]N. The durability of the catalysts was also tested with long term stability tests carried out over a period of 72+hours. Fig. 8 shows the results obtained from the three synthesized catalysts operating at their corresponding T50.
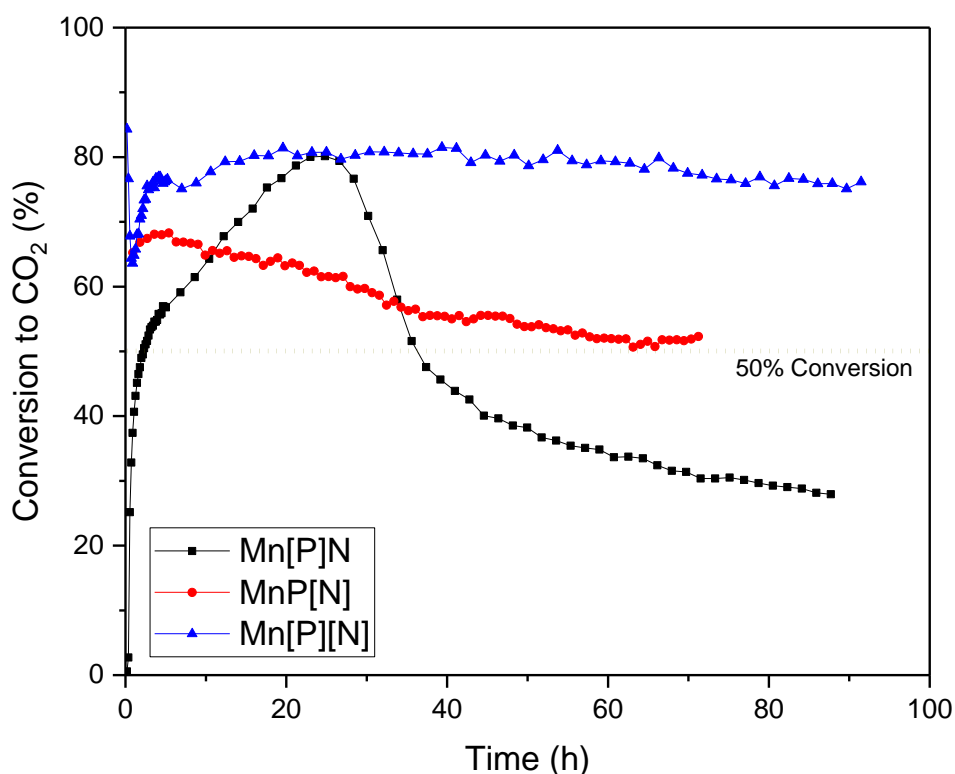
Figure 8: Long-term stability tests for Mn[P]N, MnP[N] and Mn[P][N] carried out at their corresponding T_{50}

It is interesting to see that very different behaviors are observed for each catalyst. For Mn[P]N, the conversion increases from zero to ~80% after 27 h, after which it decreases with time to reach 28% conversion after 88 h. For MnP[N], the conversion rises to ~70% after 5 h and then gradually decreases to reach a plateau of ~50% conversion. The conversion with Mn[P][N] increases to ~80% after 5 h but interestingly, tends to plateau at ~75% after 90 h of reaction. The detailed long-term stability results including the conversion to CO2, HCHO out and carbon balance for each sample are presented in the supporting information (Figs. S6, S7 and S8). For sample Mn[P]N (Fig. S6), the conversion starts from zero and then increases to about 80% within the first 27 h. The initial zero conversion might be due to the relatively low number of active sites on the catalyst surface as mentioned earlier, whereby the HCHO molecules have a higher probability to adsorb on inactive sites before reaching the active ones where oxidation

can occur. The rise to 80% conversion after 27 h may be attributed to non-renewable oxygen species and adsorbed water which are present in large quantities due to the large surface area of the catalyst. These oxygen species assist with the oxidation of HCHO molecules [20] while being consumed in the process. HCHO starts to appear in the reactor outlet after 27 h while at the same time the conversion starts decreasing down to below the expected 50% conversion (as per Fig. 7), which is attributed to complete consumption of oxygen species and deactivation of the catalyst. Characterization tests (N2 adsorption, H2-TPR and XRD see Figs. S9, S10 and S11 and Table S5 for summary, respectively) were carried out on the samples after stability testing (AST). XRD patterns show no sign of phase change for Mn[P]N-AST. For the H2-TPR results, the reduction peak temperature in the LTR remains unchanged while the reduction peak for the HTR increases from 386 °C to 401 °C. Interestingly, the AOS of Mn[P]N-AST was calculated as 3.9 compared to 3.3 for the pristine sample, possibly due to availability of more exposed sites following structural collapse of the after test sample. The BET surface area and total pore volume of Mn[P]N-AST were 187 m3 g−1 and 0.8 cm3 g−1, respectively resulting in a reduction of 21% in surface area. This points to a possible structural collapse of the hollow spheres, hence the reduction in activity during the stability test.

MnP[N] shows a more conventional stability result. The initial increase is attributed to oxygen species as well as adsorbed water on the catalyst surface. As these get consumed, the conversion gradually decreases to the expected ~50% conversion, as per the light-off curve in Fig. 7. From Fig. S7, the HCHO out behavior mirrors that of the CO2 out, i.e., HCHO out increases towards a plateau as conversion to CO2 decreases towards a plateau. However, the carbon balance still does not reach 100% due to continued adsorption on the catalyst surface. BET results for MnP[N]-AST (Fig. S9 and Table S5) show increases to the surface area and pore volume compared to the sample before test. This is possibly due to the complete removal of interlayer water after long term stability test (as opposed to degassing before N2 physisorption analysis

whereby some interlayer may still remain in the sample). This allowed more N2 molecules adsorption during physisorption testing of the AST sample and therefore higher reported BET surface area and pore volume. Indeed, the peak at ~12.5° in the XRD results for MnP[N]-AST (Fig. S11) had disappeared completely indicating the decomposition of the layered structure due to removal of structural water [67]. Also, the H2-TPR results of MnP[N]-AST show that while the LTR reduction temperature remains unchanged, the HTR reduction temperature increases to 423 °C compared to 402 °C for the pristine sample. The calculated AOS from H2 consumption was 3.7 (Table S5), which is close to the value of 3.6 recorded for the pristine sample.

Interestingly, Mn[P][N] conversion increases to about 80% after 20 h and remains at a high ~75% conversion, even after 90 h of reaction. From Fig. S8, the carbon balance follows the CO2 generation trend and no formaldehyde is seen to exit the reactor due to adsorption on the catalyst surface. The high activity of the catalyst may be due to the continuous regeneration of oxygen active species on the catalyst surface with time. BET results for Mn[P][N]-AST (Fig. S9 and Table S5) show only slight changes to the surface area and pore volume compared to the sample before test. After test XRD results in Fig. S11 show that the peak at ~12.5° disappeared for both MnP[N]-AST and Mn[P][N]-AST, which is attributed to the loss of structural water between the birnessite layers [67]. Nevertheless, after a simple water treatment (WT samples) by mixing the spent catalysts in some water followed by drying at 70 °C overnight, the resulting XRD shows that a small peak at ~12° reappeared for Mn[P][N]-AST-WT, unlike MnP[N]-AST-WT. This shows that sample Mn[P][N] has the capacity to recover its lost structural water. XPS results in Table 1 show that the ratio of K/Mn3+ for Mn[P][N] and MnP[N] are 0.12 and 0.05, respectively. The dropwise addition method can largely influence the concentration of K ions in between the layers. Therefore, when both Mn precursors are simultaneously added dropwise (as with Mn[P][N]), this ensures a more

homogeneous distribution of K ions compared to when only the Mn2+ is added dropwise (as with MnP[N]). This, in turn may facilitate the penetration of hydrated Na ions during etching treatment. This may explain the ability of Mn[P][N] to recover some of its lost structural water during stability testing. Previous work [40] has demonstrated that the presence of K in layered birnessite leads to a considerable enhancement of surface oxygen activity which then facilitates the regeneration of surface hydroxyls by activating adsorbed H2O. Since dry air is used throughout our catalytic oxidation tests, we postulate here that the adsorbed H2O comes as the byproduct of the complete oxidation of HCHO. The adsorption of water can be facilitated by hydrogen bonding with surface hydroxyls as well as hydration with the Na+ and K+ ions. It must be mentioned here that 50% conversion was expected from the light-off curve in Fig. 7. However, these light-off tests were started at high temperature (~150 °C), at which most of the structural water already evaporates. Therefore, the 50% conversion is a result of the oxidation of HCHO with lattice oxygen that get replenished by oxygen from the air (known as the Mars and van Krevelen mechanism). On the other hand, during stability test (carried out at ~84 °C), HCHO oxidation occurs via two mechanisms: (1) the Mars and van Krevelen mechanism and (2) some of the structural water remaining in the interlayers also participate in the oxidation of HCHO via the formation of hydroxyl OH groups. These hydroxyl groups then get replenished from the water formed during the complete oxidation of HCHO and adsorbed oxygen from the air ($O_2- + H_2O \rightarrow 2OH$) [19]. The fact that Mn[P][N] also has the highest content of oxygen vacancies out of all the samples (lowest Mn4+/Mn3+ ratio, Table 1) could assist with the formation of adsorbed oxygen species ($O_2 + V_o \rightarrow O_2-, O-$) [20], where V_o is an oxygen vacancy.

4. Conclusions

A low-temperature, controlled precipitation by redox (CPR) method was successfully used to synthesize MnO2 hollow spheres, using SiO2 spheres as sacrificial templates. The presented

strategy overcomes a series of drawbacks from conventional hydrothermal method such as high temperature requirement and low coating amount. The low temperature CPR method is an attractive procedure for coating of MnO2 on SiO2 templates without resorting to high temperature hydrothermal method. The three synthesized hollow spheres samples had high surface areas, hierarchical pore size distribution with high mesoporosity and presence of oxygen vacancies. Furthermore, either the γ or δ-MnO2 phase could easily be obtained by simple modification in the precursor addition protocols. Light-off experiments for the oxidation of formaldehyde showed that sample Mn[P]N performed better with T50 and T90 of 75.6 °C and 99.7 °C, respectively, under dry air, 100 ppm formaldehyde and GHSV of 30,000 h−1. The high performance of the catalyst was attributed to its highest surface area. However, long term stability tests carried out at the corresponding T50 of the three catalysts showed that sample Mn[P][N] maintained a high 75% conversion up to 90 h of reaction, instead of the expected 50% conversion. The high activity was attributed to continuous regeneration of hydroxyl species on the surface of the birnessite sheets due to the presence of a high concentration of oxygen vacancies, which helped to replenish hydroxyl radicals from the water formed during complete oxidation of formaldehyde. The results also indicate that the effect of humidity present in the air may improve the low temperature catalytic oxidation of formaldehyde via adsorption and formation of hydroxyl species on the catalyst surface.

References

[1] J.Q. Torres, S. Royer, J.P. Bellat, J.M. Giraudon, J.F. Lamonier, Formaldehyde: catalytic oxidation as a promising soft way of elimination, ChemSusChem6 (2013) 578–592, https://doi.org/10.1002/cssc.201200809.

[2] D.W. Kwon, P.W. Seo, G.J. Kim, S.C. Hong, Characteristics of the HCHO oxidation reaction over Pt/TiO2 catalysts at room temperature: the effect of relative humidity on catalytic activity, Appl. Catal. B Environ. 163 (2015) 436–443, https://doi.org/10.1016/j.apcatb.2014.08.024.

[3] X. Zhu, B. Cheng, J. Yu, W. Ho, Halogen poisoning effect of Pt-TiO2 for formaldehyde catalytic oxidation performance at room temperature, Appl. Surf. Sci. 364 (2016) 808–814, https://doi.org/10.1016/j.apsusc.2015.12.115.

[4] L. Qi, B. Cheng, J. Yu, W. Ho, High-surface area mesoporous Pt/TiO2 hollow chains for efficient formaldehyde decomposition at ambient temperature, J. Hazard. Mater. 301 (2016) 522–530, https://doi.org/10.1016/j.jhazmat.2015.09.026.

[5] H. Huang, D.Y.C. Leung, Complete oxidation of formaldehyde at room temperature using TiO2 supported metallic pd nanoparticles, ACS Catal. 1 (2011) 348–354, https://doi.org/10.1021/cs200023p.

[6] J. Zhang, Y. Li, Y. Zhang, M. Chen, L. Wang, C. Zhang, H. He, Effect of support on the activity of Ag-based catalysts for formaldehyde oxidation, Sci. Rep. 5 (2015), 12950. https://doi.org/10.1038/srep12950.

[7] C. Ma, G. Pang, G. He, Y. Li, C. He, Z. Hao, Layered sphere-shaped TiO2 capped with gold nanoparticles on structural defects and their catalysis of formaldehyde oxidation, J. Environ. Sci. (China) 39 (2016) 77–85, https://doi.org/10.1016/j.jes.2015.12.004.

[8] L. Nie, A.Meng, J. Yu,M. Jaroniec, Hierarchically macro-mesoporous Pt/γ-Al2O3 composite microspheres for efficient formaldehyde oxidation at room temperature, Sci. Rep. 3 (2013) 83997–84003, https://doi.org/10.1038/srep03215.

[9] L. Ma, D. Wang, J. Li, B. Bai, L. Fu, Y. Li, Ag/CeO2 nanospheres: efficient catalysts for formaldehyde oxidation, Appl. Catal. B Environ. 148–149 (2014) 36–43, https://doi.org/10.1016/j.apcatb.2013.10.039.

[10] G. Pang, D. Wang, Y. Zhang, C. Ma, Z. Hao, Catalytic activities and mechanism of formaldehyde oxidation over gold supported on MnO2 microsphere catalysts at room temperature, Front. Environ. Sci. Eng. 10 (2016) 447–457, https://doi.org/10.1007/s11783-015-0808-8.

[11] C. Zhang, H. He, A comparative study of TiO2 supported noble metal catalysts for the oxidation of formaldehyde at room temperature, Catal. Today 126 (2007) 345–350, https://doi.org/10.1016/j.cattod.2007.06.010.

[12] X. LIU, J. LU, K. QIAN, W. HUANG, M. LUO, A comparative study of formaldehyde and carbon monoxide complete oxidation on MnOx-CeO2 catalysts, J. Rare Earths 27 (2009) 418–424, https://doi.org/10.1016/S1002-0721(08)60263-X.

[13] J.Q. Torres, J.-M. Giraudon, J.-F. Lamonier, Formaldehyde total oxidation over mesoporous MnOx catalysts, Catal. Today 176 (2011) 277–280, https://doi.org/10.1016/j.cattod.2010.11.089.

[14] C. Ma, D. Wang, W. Xue, B. Dou, H. Wang, Z. Hao, Investigation of formaldehyde oxidation over Co3O4 −CeO2 and au/Co3O4 −CeO2 Catalysts at room temperature: effective removal and determination of reaction mechanism, Environ. Sci. Technol. 45 (2011) 3628–3634, https://doi.org/10.1021/es104146v.

[15] J. Quiroz, J.M. Giraudon, A. Gervasini, C. Dujardin, C. Lancelot, M. Trentesaux, J.F. Lamonier, Total oxidation of formaldehyde over MnOx-CeO2 catalysts: the effect of acid treatment, ACS Catal. 5 (2015) 2260–2269, https://doi.org/10.1021/cs501879j.

[16] Y. Sekine, Oxidative decomposition of formaldehyde by metal oxides at room temperature, Atmos. Environ. 36 (2002) 5543–5547, https://doi.org/10.1016/S1352- 2310(02)00670-2.

[17] S. Rong, P. Zhang, Y. Yang, L. Zhu, J. Wang, F. Liu,MnO2 framework for instantaneous mineralization of carcinogenic airborne formaldehyde at room temperature, ACS Catal. 7 (2017) 1057–1067, https://doi.org/10.1021/acscatal.6b02833.

[18] J. Wang, G. Zhang, P. Zhang, Layered birnessite-type MnO2 with surface pits for enhanced catalytic formaldehyde oxidation activity, J. Mater. Chem. A 5 (2017) 5719–5725, https://doi.org/10.1039/C6TA09793F.

[19] J. Zhou, L. Qin, W. Xiao, C. Zeng, N. Li, T. Lv, H. Zhu, Oriented growth of layered-MnO2 nanosheets over A-MnO2 nanotubes for enhanced room-temperature HCHO oxidation, Appl. Catal. B Environ. 207 (2017) 233–243, https://doi.org/10.1016/j.apcatb. 2017.01.083.

[20] J. Wang, J. Li, C. Jiang, P. Zhou, P. Zhang, J. Yu, The effect of manganese vacancy in birnessite-type MnO2 on room-temperature oxidation of formaldehyde in air, Appl. Catal. B Environ. 204 (2017) 147–155, https://doi.org/10.1016/j.apcatb.2016.11.036.

[21] J. Zhang, Y. Li, L. Wang, C. Zhang, H. He, Catalytic oxidation of formaldehyde over manganese oxides with different crystal structures, Catal. Sci. Technol. 5 (2015) 2305–2313, https://doi.org/10.1039/C4CY01461H.

[22] B. Bai, J. Li, J. Hao, 1D-MnO2, 2D-MnO2 and 3D-MnO2 for low-temperature oxidation of ethanol, Appl. Catal. B Environ. 164 (2015) 241–250, https://doi.org/10.1016/j.apcatb.2014.08.044.

[23] G. Zhu, J. Zhu, W. Jiang, Z. Zhang, J. Wang, Y. Zhu, Q. Zhang, Surface oxygen vacancy induced α-MnO2 nanofiber for highly efficient ozone elimination, Appl. Catal. B Environ. 209 (2017) 729–737, https://doi.org/10.1016/j.apcatb.2017.02.068.

[24] W. Si, Y. Wang, Y. Peng, X. Li, K. Li, J. Li, A high-efficiency γ-MnO2 -like catalyst in toluene combustion, Chem. Commun. 51 (2015) 14977–14980, https://doi.org/10.1039/C5CC04528B.

[25] H. Chen, Y. Wang, Y.-K. Lv, Catalytic oxidation of NO over MnO2 with different crystal structures, RSC Adv. 6 (2016) 54032–54040, https://doi.org/10.1039/C6RA10103H.

[26] B. Zhang, G. Cheng, W. Ye, X. Zheng, H. Liu, M. Sun, L. Yu, Y. Zheng, X. Cheng, Rational design of MnO2 @MnO2 hierarchical nanomaterials and their catalytic activities, Dalt. Trans. 45 (2016) 18851–18858, https://doi.org/10.1039/C6DT03523J.

[27] Y. Boyjoo, M. Wang, V.K. Pareek, J. Liu, M. Jaroniec, Synthesis and applications of porous non-silica metal oxide submicrospheres, Chem. Soc. Rev. 45 (2016) 6013–6047, https://doi.org/10.1039/C6CS00060F.

[28] J. Wang, H. Tang, H. Wang, R. Yu, D. Wang, Multi-shelled hollow micro-/nanostructures: promising platforms for lithium-ion batteries, Mater. Chem. Front. 1 (2017) 414–430, https://doi.org/10.1039/C6QM00273K.

[29] M. Chen, J. Wang, H. Tang, Y. Yang, B. Wang, H. Zhao, D. Wang, Synthesis of multishelled MnO2 hollow microspheres via an anion-adsorption process of hydrothermal intensification, Inorg. Chem. Front. 3 (2016) 1065–1070, https://doi.org/10.1039/C6QI00083E.

[30] T. Liu, C. Jiang, W. You, J. Yu, Hierarchical porous C/MnO2 composite hollow microspheres with enhanced supercapacitor performance, J. Mater. Chem. A 5 (2017) 8635–8643, https://doi.org/10.1039/C7TA00363C.

[31] X. Tang, Z.H. Liu, C. Zhang, Z. Yang, Z. Wang, Synthesis and capacitive property of hierarchical hollow manganese oxide nanospheres with large specific surface area, J. Power Sources 193 (2009) 939–943, https://doi.org/10.1016/j.jpowsour.2009.04.037.

[32] D. Portehault, S. Cassaignon, E. Baudrin, J.P. Jolivet, Structural and morphological control of manganese oxide nanoparticles upon soft aqueous precipitation through MnO4 − /Mn2 + reaction, J. Mater. Chem. A 19 (2009) 2407–2416, https://doi.org/10.1039/B816348K.

[33] J.E. Post, Manganese oxide minerals: crystal structures and economic and environmental significance, Proc. Natl. Acad. Sci. 96 (1999) 3447–3454, https://doi.org/10.1073/pnas.96.7.3447.

[34] M. Wang, H. Liu, Z.H. Huang, F. Kang, Activated carbon fibers loaded with MnO2 for removing no at room temperature, Chem. Eng. J. 256 (2014) 101–106, https://doi.org/10.1016/j.cej.2014.06.108.

[35] X. Fu, J. Feng, H. Wang, K.M. Ng, Morphological and structural evolution of α-MnO2 nanorods synthesized via an aqueous route through MnO4 − /Mn2 + reaction, J. Solid State Chem. 183 (2010) 883–889, https://doi.org/10.1016/j.jssc.2010.02.002.

[36] X. Fu, J. Feng, H. Wang, K.M. Ng, Manganese oxide hollow structures with different phases: synthesis, characterization and catalytic application, Catal. Commun. 10 (2009) 1844–1848, https://doi.org/10.1016/j.catcom.2009.06.013.

[37] L. Liu, Y. Luo, W. Tan, Y. Zhang, F. Liu, G. Qiu, Facile synthesis of birnessite-type manganese oxide nanoparticles as supercapacitor electrode materials, J. Colloid Interf. Sci. 482 (2016) 183–192, https://doi.org/10.1016/j.jcis.2016.07.077.

[38] S. Zhao, T. Liu, D. Hou, W. Zeng, B. Miao, S. Hussain, X. Peng, M.S. Javed, Controlled synthesis of hierarchical birnessite-type MnO2 nanoflowers for supercapacitor applications, Appl. Surf. Sci. 356 (2015) 259–265, https://doi.org/10.1016/j.apsusc.2015.08.037.

[39] H. Tian, J. He, L. Liu, D. Wang, Z. Hao, C. Ma, Highly active manganese oxide catalysts for low-temperature oxidation of formaldehyde, Microporous Mesoporous Mater. 151 (2012) 397–402, https://doi.org/10.1016/j.micromeso.2011.10.003.

[40] J. Wang, D. Li, P. Li, P. Zhang, Q. Xu, J. Yu, Layered manganese oxides for formaldehyde-oxidation at room temperature: the effect of interlayer cations, RSC Adv. 5 (2015) 100434–100442, https://doi.org/10.1039/C5RA17018D.

[41] X. Duan, J. Yang, H. Gao, J. Ma, L. Jiao, W. Zheng, Controllable hydrothermal synthesis

of manganese dioxide nanostructures: shape evolution, growth mechanism and electrochemical properties, CrystEngComm 14 (2012) 4196, https://doi.org/10.1039/c2ce06587h.

[42] A.A. Radhiyah, M. Izan Izwan, V. Baiju, C. Kwok Feng, I. Jamil, R. Jose, Doubling of electrochemical parameters via the pre-intercalation of Na+ in layered MnO2 nanoflakes compared to α-MnO2 nanorods, RSC Adv. 5 (2015) 9667–9673, https://doi.org/10.1039/C4RA15536J.

[43] C. Julien, M. Massot, R. Baddour-Hadjean, S. Franger, S. Bach, J.P. Pereira-Ramos, Raman spectra of birnessite manganese dioxides, Solid State Ionics 159 (2003) 345–356, https://doi.org/10.1016/S0167-2738(03)00035-3.

[44] C. Julien, M. Massot, S. Rangan, M. Lemal, D. Guyomard, Study of structural defects in γ-MnO2 by Raman spectroscopy, J. Raman Spectrosc. 33 (2002) 223–228, https://doi.org/10.1002/jrs.838

[45] C.M. Julien, M. Massot, C. Poinsignon, Lattice vibrations of manganese oxides: part I. Periodic structures, Spectrochim. Acta A Mol. Biomol. Spectrosc. 60 (2004) 689–700, https://doi.org/10.1013/S1386-1425(03)00279-8.

[46] D.T. Zahn, Vibrational spectroscopy of bulk and supported manganese oxides, Phys. Chem. Chem. Phys. 1 (1999) 185–190, https://doi.org/10.1039/A807821A.

[47] R. Baddour-Hadjean, J.P. Pereira-Ramos, Raman micro spectrometry applied to the study of electrode materials for lithium batteries, Chem. Rev. 110 (2009) 1278–1319, https://doi.org/10.1021/cr800344k.

[48] C. Julien, M. Massot, Spectroscopic studies of the local structure in positive electrodes for lithium batteries, Phys. Chem. Chem. Phys. 4 (2002) 4226–4235, https://doi.org/10.1021/cm011623u.

[49] J.E. Post, D.R. Veblen, Crystal structure determinations of synthetic sodium, magnesium, and potassium birnessite using TEM and the Rietveld method, Am. Mineral. 75 (1990) 477–489.

[50] J. Yang, M. Ma, C. Sun, Y. Zhang, W. Huang, X. Dong, Hybrid $NiCo_2S_4$ @MnO_2 heterostructures for high-performance supercapacitor electrodes, J. Mater. Chem. A 3 (2015) 1258–1264, https://doi.org/10.1039/C4TA05747C.

[51] Z.C. Yang, C.H. Tang, H. Gong, X. Li, J. Wang, Hollow spheres of nanocarbon and their manganese dioxide hybrids derived from soft template for supercapacitor application, J. Power Sources 240 (2013) 713–720, https://doi.org/10.1016/j.jpowsour.2013.05.034.

[52] L. Liu, H. Tian, J. He, D. Wang, Q. Yang, Preparation of birnessite-supported Pt nanoparticles and their application in catalytic oxidation of formaldehyde, J. Environ. Sci. (China) 24 (2012) 1117–1124, https://doi.org/10.1016/S1001-0742(11)60879-6.

[53] X. Chen, Y.F. Shen, S.L. Suib, C.L. O'Young, Characterization of manganese oxide octahedral molecular sieve (M-OMS-2) materials with different metal cation dopants, Chem. Mater. 14 (2002) 940–948, https://doi.org/10.1021/cm000868o.

[54] M. Huang, R. Mi, H. Liu, F. Li, X.L. Zhao, W. Zhang, S.X. He, Y.X. Zhang, Layered manganese oxides-decorated and nickel foam-supported carbon nanotubes as advanced binder-free supercapacitor electrodes, J. Power Sources 269 (2014) 760–767, https://doi.org/10.1016/j.jpowsour.2014.07.031.

[55] Z. Liu, K. Xu, H. Sun, S. Yin, One-step synthesis of single-layer MnO2 nanosheets with multi-role sodium dodecyl sulfate for high-performance pseudocapacitors, Small 11 (2015) 2182–2191, https://doi.org/10.1002/smll.201402222.

[56] M.C. Biesinger, B.P. Payne, A.P. Grosvenor, L.W.M. Lau, A.R. Gerson, R.S.C. Smart, Resolving surface chemical states in XPS analysis of first row transition metals, oxides and hydroxides: Cr, Mn, Fe, Co and Ni, Appl. Surf. Sci. 257 (2011) 2717–2730, https://doi.org/10.1016/j.apsusc.2010.10.051.

[57] X. Liang, C. Hart, Q. Pang, A. Garsuch, T. Weiss, L.F. Nazar, A highly efficient polysulfide mediator for lithium-sulfur batteries, Nat. Commun. 6 (2015) 1–8, https://doi.org/10.1038/ncomms6682.

[58] H.W. Nesbitt, D. Banerjee, Interpretation of XPS Mn(2p) spectra of Mn oxyhydroxides and constraints on the mechanism of MnO2 precipitation, Am. Mineral. 83 (1998) 305–315, https://doi.org/10.2138/am-1998-3-414.

[59] Y. Ma, S.G. Wang, M. Fan, W.X. Gong, B.Y. Gao, Characteristics and defluoridation performance of granular activated carbons coated with manganese oxides, J. Hazard. Mater. 168 (2009) 1140–1146, https://doi.org/10.1016/j.jhazmat.2009.02.145.

[60] J. Liu, X. Ge, X. Ye, G. Wang, H. Zhang, H. Zhou, Y. Zhang, H. Zhao, 3D graphene/δ-MnO2 aerogels for highly efficient and reversible removal of heavy metal ions, J. Mater. Chem. A 4 (2016) 1970–1979, https://doi.org/10.1039/C5TA08106H.

[61] J. Wang, R. Yunus, J. Li, P. Li, P. Zhang, J. Kim, In situ synthesis of manganese oxides on polyester fiber for formaldehyde decomposition at room temperature, Appl. Surf. Sci. 357 (2015) 787–794, https://doi.org/10.1016/j.apsusc.2015.09.109.

[62] Y. Meng, W. Song, H. Huang, Z. Ren, S.Y. Chen, S.L. Suib, Structure-property relationship of bifunctional MnO2 nanostructures: highly efficient, ultra-stable electrochemical water oxidation and oxygen reduction reaction catalysts identified in alkaline media, J. Am. Chem. Soc. 136 (2014) 11452–11464, https://doi.org/10.1021/ja505186m.

[64] V.P. Santos, M.F.R. Pereira, J.J.M. Orfao, J.L. Figueiredo, Synthesis and characterization of manganese oxide catalysts for the total oxidation of ethyl acetate, Top. Catal. 52 (2009) 470–481, https://doi.org/10.1007/s11244-009-9187-3.

[66] M. Xu, L. Kong, W. Zhou, H. Li, Hydrothermal synthesis and pseudo capacitance properties of α-MnO2 hollow spheres and hollow urchins, J. Phys. Chem. C 111 (2007) 19141–19147, https://doi.org/10.1021/jp076730b.

[67] L. Liu, H. Tian, J. He, D. Wang, Q. Yang, Preparation of birnessite-supported Pt nanoparticles and their application in catalytic oxidation of formaldehyde, J. Environ. Sci. (China) 24 (2012) 1117–1124, https://doi.org/10.1016/S1001-0742(11)60879-6.